Mon. Not. R. Astron. Soc. **000**, 1–14 (2002) Printed 1 April 2015 (MN LATEX style file v2.2)

The variation in molecular gas depletion time among nearby galaxies: II the impact of galaxy internal structures

Mei-Ling Huang[1⋆], Guinevere Kauffmann[1]
[1]*Max-Planck Institute for Astrophysics, Karl-Schwarzschild-Str. 1, D-85748 Garching, Germany*

arXiv:1412.3111v2 [astro-ph.GA] 30 Mar 2015

in original form 2014 Sep

ABSTRACT

We use a data set of nearby galaxies drawn from the HERACLES, ATLAS^{3D}, and COLD GASS surveys to study variations in molecular gas depletion time (t_{dep}) in galaxy structures such as bulges, grand-design spiral arms, bars and rings. Molecular gas is traced by CO line emission and star formation rate (SFR) is derived using the combination of far-ultraviolet and mid-infrared (MIR) data. The contribution of old stars to MIR emission for the ATLAS^{3D} sample is corrected using 2MASS K-band images. We apply a two-dimensional image decomposition algorithm to decompose galaxies into bulges and discs. Spiral arms, bars and rings are identified in the residual maps, and molecular gas depletion times are derived on a square grid of 1 kpc^2 size. In previous work, we showed that t_{dep} correlates strongly with specific star formation rate (sSFR). We now find that at a given sSFR, the bulge has shorter t_{dep} than the disc. The shift to shorter depletion times is most pronounced in the inner bulge ($R < 0.1R_e$). Grids from galaxies with bars and rings are similar to those from galactic bulges in that they have reduced t_{dep} at a given sSFR. In contrast, the t_{dep} versus sSFR relation in the discs of galaxies with spiral arms is displaced to longer t_{dep} at fixed sSFR. We then show that the differences in the t_{dep}−sSFR relation for bulges, discs, arms, bars and rings can be linked to variations in *stellar*, rather than gas surface density between different structures. Our best current predictor for t_{dep}, both globally and for 1 kpc grids, is given by $t_{dep} = -0.36\log(\Sigma_{\rm SFR}) - 0.50\log(\Sigma_*) + 5.87$.

Key words: galaxy formation

1 INTRODUCTION

Numerous studies have attempted to understand how gas is converted into stars. Observational data indicate a power-law relation between these two quantities:

$$\Sigma_{\rm SFR} \propto \Sigma_{\rm gas}^{\rm N},$$

where $\Sigma_{\rm SFR}$ and $\Sigma_{\rm gas}$ are the star formation rate (SFR) and gas surface densities in units of $M_\odot$ yr^{-1} kpc^{-2} and $M_\odot$ pc^{-2}. Such relations are often called the Kennicutt-Schmidt (K-S) laws (Schmidt 1959; Kennicutt 1998).

Only recently have observations provided high-resolution, multiwavelength images of nearby galaxies for spatially-resolved, sensitive measurements of $\Sigma_{\rm gas}$ and $\Sigma_{\rm SFR}$, allowing exploration of the K-S relation on sub-kpc scales. For instance, Bigiel et al. (2008, 2011) used the CO(J=2-1) line as an H_2 gas tracer and far-ultraviolet (FUV) plus 24μm emission as a SFR tracer to study the K-S relation at sub-kpc resolution in nearby disc galaxies observed as part of the HERA CO-Line Extragalactic Survey (HERACLES; Leroy et al. 2008). They proposed a linear K-S relation (and thus a constant molecular gas depletion time (t_{dep})), independent of local conditions such as orbital timescale, mid-plane gas pressure and disc stability parameter Q (Leroy et al. 2008). Some subsequent works, however, reported non-linear relations between $\Sigma_{\rm SFR}$ and $\Sigma_{\rm H_2}$ using different fitting methods (Shetty et al. 2013) or new data (e.g., Momose et al. 2013; Pan et al. 2014).

Saintonge et al. (2011b) investigated the relation between integrated molecular gas depletion time and global galaxy parameters statistically using galaxies observed as part of the COLD GASS project, which obtained IRAM ∼22″ single beam CO(1-0) line measurements for ∼360 galaxies with stellar masses $10^{10} - 10^{11.5} M_\odot$ in the redshift range 0.02 – 0.05 (Saintonge et al. 2011a). SFR was estimated by fitting stellar population models to optical and ultraviolet (UV) broad-band photometry. An estimate of the molecular gas depletion time of the full galaxy was made by applying aperture corrections to the CO line luminosities. Molecular gas depletion time was found to correlate well

⋆ E-mail: mlhuang@mpa-garching.mpg.de

with various galaxy parameters such as stellar mass, stellar surface density, concentration of the light (i.e., bulge-to-disc ratio), near-UV (NUV)−r color and specific star formation rate (sSFR; defined as the ratio of SFR to stellar mass).

We subsequently improved on this work by estimating SFR with the combination of GALEX FUV and WISE 22μm data within fixed apertures matched to the 22″ beam size of the gas observations (Huang & Kauffmann 2014). Dependences of the depletion time on galaxy structural parameters such as stellar surface density and concentration index were then found to be much weaker, or even absent. We went on to demonstrate that the *primary dependence* of t_{dep} is on sSFR. All other remaining correlations, such as the t_{dep}–stellar mass relation, were demonstrated to be secondary, i.e., induced by the fact that sSFR in turn correlates with a variety of other global galaxy parameters. We note that a comprehensive study based on 500 star forming galaxies at redshifts from z = 0 to 3 also supports our findings (Genzel et al. 2014).

We also compared the results obtained from the COLD GASS galaxies to estimates of t_{dep} on 1 kpc scales using high-resolution CO and SFR maps from the HERACLES survey. The global t_{dep}–sSFR relation derived from the COLD GASS sample and that derived from 1 kpc grids placed on HERACLES galaxies agree remarkably well. This suggests that the local molecular gas depletion time is dependent on the local fraction of young-to-old stars and that galaxies with high current-to-past-averaged star formation activity, will consume their molecular gas reservoir sooner.

Another aspect that has not been fully understood is the role of galaxy structures such as bulges, arms, bars, or rings in determining the molecular gas depletion time. We note that simply using all available grids from the whole galaxy or integrated values of gas mass and SFR to study molecular gas depletion times might smooth out variations caused by different structures.

Many studies have investigated whether the star formation efficiency (SFE) varies in differnt galactic environments. For instance, Meidt et al. (2013) studied the inner region of the spiral galaxy M51 with a high resolution CO (1-0) map (∼40 pc) and proposed that streaming motions, induced by gravitational instabilities due to bars and arms, cause variations in gas depletion time. Momose et al. (2010) observed a barred spiral galaxy, NGC 4303, with CO (1-0) observations and found that its arms have twice higher SFEs than its bar, although strong CO emission is both seen in the bar and the disc region along the arms. Fujimoto et al. (2014) proposed that these results could be understood in a model where star formation is regulated by collisions between molecular clouds. However, other studies have come to the opposite conclusion about the viability of the cloud collision model (Foyle et al. 2010; Eden et al. 2012). Other observational studies using CO(1-0) line luminosities as the gas tracer and Hα or 24μm luminosities as the SFR tracer have demonstrated that the SFE in spiral arms is enhanced compared to regions outside the arms (e.g., Lord & Young 1990; Knapen et al. 1996; Rebolledo et al. 2012; Hirota et al. 2014).

We note that most of these studies explored the influence of structures on SFE based on samples of one or only a few galaxies, and they did not consider variations in SFE with respect to the t_{dep}−sSFR relation. In this paper, we try to understand whether galaxy structures induce significant variation in molecular gas depletion time by systematically separating the grids into those in bulge, arm, bar, and ring regions, and by studying how the local depletion time from these different regions varies with respect to the established t_{dep}−sSFR relation.

Our paper is organized as follows. We describe the multiwavelength data sets used in this work in Section 2, and our methods for identifying galaxy structures and deriving t_{dep} and sSFR on local scales in Section 3. Our results are presented in Section 4, where we look at the t_{dep}–sSFR relations for the grids in the bulge, arm, bar, and ring regions respectively. Finally, we compare our results with previous studies and discuss our findings in Section 5.

2 DATA

In this section we introduce the data sets we use in this work. The HERACLES sample provides spatially-resolved CO maps with resolution $\lesssim$ 1kpc, appropriate for pixel-by-pixel studies. Because of this good resolution, we are able to identify the pixels lying in galaxy structures such as bulges or spiral arms. ATLAS^{3D} galaxies are mostly early-type galaxies and are included because this data supplements the number of data points we are able to extract from the bulge-dominated regions of galaxies. The COLD GASS project targets more distant sources and therefore provides only integrated values of the molecular gas mass. Nevertheless, the large sample size gives us the opportunity to carry out a statistical analysis of global relations between gas depletion time and other galaxy properties.

2.1 HERACLES

To study molecular gas depletion time on sub-kpc scales, we use public data from the HERA CO-Line Extragalactic Survey (HERACLES; Leroy et al. 2008). HERACLES has released CO ($J = 2 - 1$) maps for 48 nearby galaxies, achieving a spatial resolution ∼13 arcsec and an average H_2 surface density detection limit of $\sim 3\ M_\odot pc^{-2}$. We analyze 21 massive galaxies with log $(M_*/M_\odot) \geqslant 10$ from the catalog in Leroy et al. (2013) so that we avoid those low-mass galaxies with less reliable H_2 mass measurements. All our selected galaxies are located within a distance of ∼20 Mpc.

A variety of ancillary data is available for the HERACLES sample, which allow us to derive the SFR and stellar mass surface densities. The relevant data includes FUV images from GALEX All-sky Imaging survey (AIS) and Nearby Galaxy Survey (NGS; Gil de Paz et al. 2007), 24 μm data from the Spitzer Infrared Nearby Galaxies Survey (SINGS; Kennicutt et al. 2003), HI maps from The HI Nearby Galaxies Survey (THINGS; Walter et al. 2008), and optical images from Sloan Digital Sky Survey (SDSS). FUV images from GALEX satellite have effective wavelength 1528 Å and angular resolution ∼4.3 arcsec FWHM. SINGS provides MIPS 24μm images with an angular resolution ∼6 arcsec and 3 σ sensitivity ∼0.21 MJy sr^{-1}. The maps (natural-weighting) from THINGS have an angular resolution of ∼11 arcsec and are sensitive to $\Sigma_{\rm HI} \geqslant 0.5\ M_\odot\ pc^{-2}$.

Combining these public data sets, we estimate gas, SFR, and stellar mass surface densities as a function of position in

the galaxy by dividing the galaxy into a set of square cells with 1 kpc^2 size. In this way, we are able to separate the grids within bulges, arms, bars, rings from those in the rest of the galaxy. Galaxy parameters such as distance, inclination angle, position angle are taken directly from Leroy et al. (2013).

2.2 ATLAS^{3D}

To increase the amount of data in bulge regions, we make use of a subset of the galaxies observed as part of the ATLAS^{3D} project (Cappellari et al. 2011), with publicly-available resolved interferometric CO(1-0) maps (Alatalo et al. 2013). The full ATLAS^{3D} sample consists of a volume-limited sample of 260 nearby early-type (elliptical E and lenticular S) galaxies (ETGs) with a cut-off absolute magnitude of $M_K = -21.5$. The ATLAS^{3D} galaxies were observed in CO(1-0) and CO(2-1) by the IRAM 30m telescope (Young et al. 2011), and those with detected CO integrated fluxes larger than 19 Jy kms^{-1} were imaged using the Combined Array for Research in Millimeter Astronomy (CARMA) (Alatalo et al. 2013). This data set includes 30 ETGs. Together with 10 CO-detected galaxies that have interferometric CO(1-0) data from the literature, there are a total 40 ETGs with resolved CO maps in the ATLAS^{3D} sample. The reader is referred to Alatalo et al. (2013) for further details about the sample, the observations and the analyses.

We derive SFR using the combination of FUV emission from GALEX data and mid-infrared emission at 22μm from WISE data. The FUV maps are retrieved from GALEX Data Release 7 products. When several atlas images from different observing programs are available, we always use the one with the longest exposure time. The exposure time for ∼2/3 of the sample is longer than 1500 seconds; the rest of galaxies have data from the AIS program with typical exposure time ∼100 – 200 seconds and limiting magnitude ∼20.5 AB magnitude. There are 3 galaxies without FUV observations from GALEX. WISE provides 22μm images of the whole sky, with angular resolution 12 arcsec and 5σ point-source sensitivity ∼ 6mJy. All galaxies have WISE observations. The stellar mass is derived from SDSS 5-band images using a SED-fitting method; the SDSS images are downloaded from SDSS Data Release 9.

In Figure 1 we compare the basic properties of the galaxies in the HERACLES and ATLAS^{3D} samples. Generally, their stellar masses are comparable. The HERACLES galaxies are much closer than the ATLAS^{3D} galaxies, so the angular disc sizes (R_{25}) of the former sample are larger than the latter sample. The distributions of the concentration index, R_{90}/R_{50}, which is tightly related to the bulge-to-disc ratio of the galaxy (Gadotti et al. 2009; Weinmann et al. 2009), reflect the fact that the ATLAS^{3D} galaxies are mostly ETGs and the HERACLES sample consists of mostly disc galaxies.

2.3 COLD GASS

The sample is drawn from the COLD GASS survey catalogue (Saintonge et al. 2011a,b, 2012), which contains CO ($J = 1-0$) line measurements from the IRAM 30m telescope for ∼360 nearby galaxies with stellar masses in the range

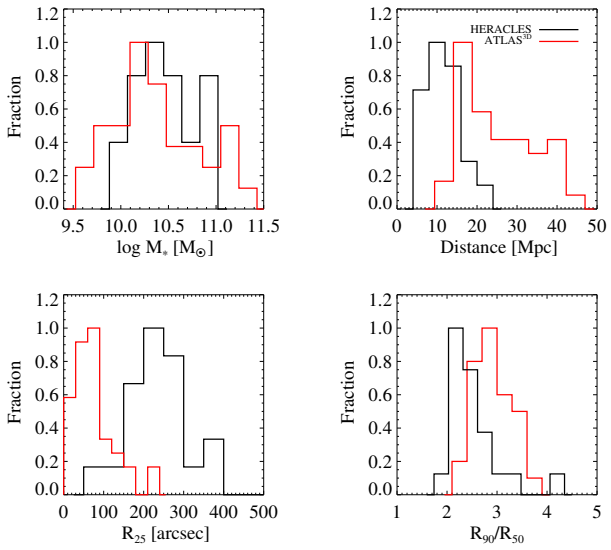

Figure 1. Comparison of stellar mass, distance, B-band isophotal radius at 25 mag arcsec^{-2} (R_{25}), concentration index (R_{90}/R_{50}) for HERACLES galaxies (black line) and ATLAS^{3D} galaxies (red line).

$10^{10} - 10^{11.5} M_\odot$ and redshifts in the range $0.025 < z < 0.05$. We only select the galaxies with detected CO fluxes in our studies. The reader is referred to Saintonge et al. (2011a) for a detailed description of the sample selection and the observations.

In the same fashion as was done for the ATLAS^{3D} sample, we derive SFR by summing GALEX FUV and WISE 22μm luminosities and we estimate stellar mass by fitting stellar population synthesis models to SDSS 5-band images. We retrieve the FUV maps from GALEX Data Release 7 products; the maps with the longest exposure time are always preferred. Most of our FUV images are from the Medium Imaging survey (MIS) with typical exposure time ∼1500 seconds; 81 out of 366 galaxies only have data from the AIS program with typical exposure time ∼100 – 200 seconds. The limiting magnitude for MIS is 23.5 AB magnitude and for AIS, it is 20.5 AB magnitude. All galaxies have both WISE and SDSS imaging data.

3 METHODS

Molecular gas depletion time is defined as $\Sigma_{H_2}/\Sigma_{SFR}$ or M_{H_2}/SFR, where Σ_{H2} and Σ_{SFR} are molecular gas and SFR surface densities, and M_{H2} is molecular gas mass. Specific SFR (sSFR) is defined as SFR/M_* or Σ_{SFR}/Σ_*, where Σ_* is stellar mass surface density. We use the first definition for the spatially-resolved HERACLES sample; the second definition is used for the ATLAS^{3D} and COLD GASS samples to derive an integrated depletion time and sSFR.

3.1 Overview of the spatial scales probed by the observations

For the HERACLES sample, the spatial resolution of the CO maps is ∼13″ , which is ≲1kpc. The GALEX FUV and

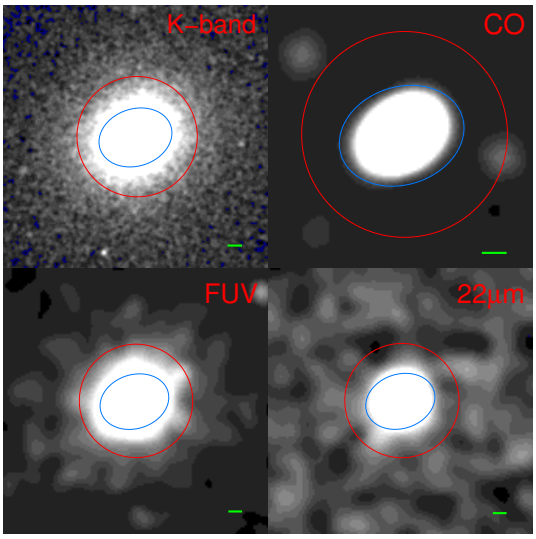

Figure 2. 2MASS K-band (upper left), CARMA CO (upper right), GALEX FUV (lower left) and WISE 22μm (lower right) maps for NGC3607 in the ATLAS^{3D} sample. All maps are convolved to 13 arcsec resolution. The blue ellipses and red circles indicate the aperture derived from CO(1-0) map and the half-light radius R_e in K-band taken from Cappellari et al. (2011). The green bar shows the physical scale of 1kpc in each map.

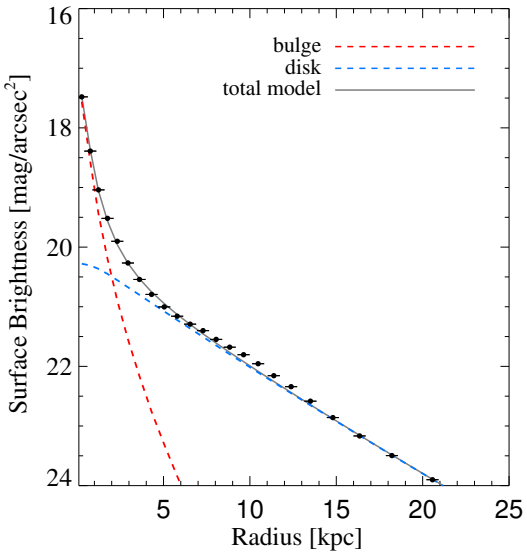

Figure 3. An example of a one-dimensional decomposition profile for a galaxy in the HERACLES sample. Black points show the mean surface brightness of the g-band image in elliptical annuli with the axial ratio and position angle drawn from the disc model. The grey line denotes the total model flux. The red and blue dashed lines denote the model fluxes for the bulge and the disc.

Spitzer 24μm maps have better resolution, so we degrade them to the same resolution as the CO maps. The sizes of structures we want to study, such as bulges, arms, bars and rings, are well-resolved with 1kpc smoothing. We therefore use 1kpc × 1kpc grid cells as our sampling elements.

ATLAS^{3D} includes a subset of ∼40 ETGs with resolved CO maps and supplements data for bulge regions. Given that the size of the CO-emitting regions is only a few kpcs or even smaller and that the gas surface density sensitivity limit varies from one galaxy to another for the ATLAS^{3D} project, we do not derive the depletion time within 1kpc^2 grids, but within the CO-emitting region. We first smooth CO maps to the same 13″ resolution as the WISE image. We run SEXTRACTOR on the CO moment0 maps and use the Kron aperture as the size of CO-emitting region. The CO flux within the Kron aperture is converted to the molecular gas mass by applying a Galactic CO-to-H_2 conversion factor. We note that we measure the SFR and the stellar mass using the same aperture as the CO emission. An example of our multi-band images with the aperture derived from the CO map is shown in Figure 2.

The CO emission for the COLD GASS galaxies is observed within the IRAM 22″ Gaussian beam. Once again, SFR must be measured within the same region where molecular gas is observed; thus, we derive SFR for the COLD GASS galaxies by placing a 22″ Gaussian beam on the FUV and 22μm maps. As pointed out in Huang & Kauffmann (2014), the depletion timescales that we derive for the COLD GASS galaxies agree better with the HERACLES results than those in Saintonge et al (2011b).

3.2 Identification of bulges/arms/bars/rings

In this section, we fit Sérsic models to SDSS g-band images and identify bars/rings/spiral arms from the residual images. After the main features of galaxies, i.e. the bulge and the disc, are removed, the residual maps can reveal fine structures such as rings or arms more clearly.

We first mask stars and background galaxies in the SDSS images using the colour-based masks described in (Muñoz-Mateos et al. 2009). We inspect the images again and mask stars by hand when necessary. The masked regions are marked as bad pixels which will not be used for fitting. The maps of Schlegel et al. (1998) are used to correct for Galactic extinction. We next apply a two-dimensional image decomposition program called GALFIT (Peng et al. 2002) to the SDSS g-band images to decompose galaxies into bulges and disks. To fit the luminosity profile of the galaxies, the code assumes a two-component model, Sérsic bulge plus Sérsic disk profile, where the Sérsic n values for the bulge and disk are allowed to vary from 1.5 to 4 and from 0.8 to 1.2, respectively. The grids within the effective radius of the bulge model are designated as the bulge grids. One example of the fitting result is shown in Figure 3. The surface brightness profile of the galaxy is clearly separated into two components. The effective radii of the bulge and disc are 0.8 and 8.0 kpc.

We identify seven galaxies with large arms, three barred galaxies, and one galaxy with a ring from the residual maps. We visually select grids within the arm, bar and ring regions. Examples are shown in Figure 4. Note that we exclude those grids with Σ_{H_2} below the CO detection sensitivity limit or $\Sigma_{SFR} < 10^{-3}$ $M_\odot$ yr^{-1} kpc^{-2}, because the SFR calibration does not work for these low values (see Section 3.4.1). As can

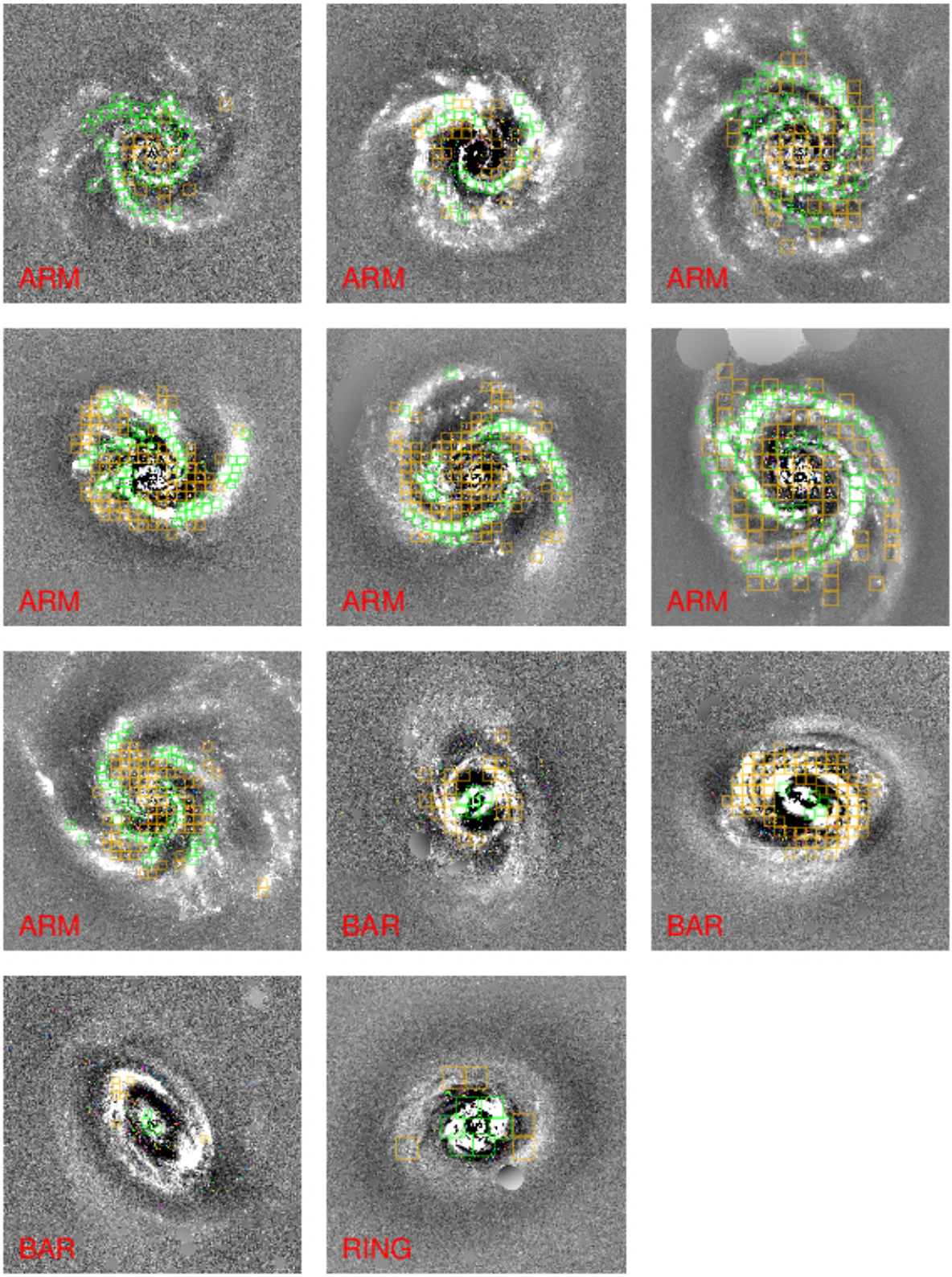

Figure 4. SDSS g-band residual maps for HERACLES galaxies with grand-design spiral arms, bars and rings. Coloured squares show grids of 1-kpc^2 size in the area of the targeted structure (green) and in the rest of the galaxy (yellow) . Note that we only show the grids that lie above the gas and SFR sensitivity limits.

be seen, we are able to sample between $50 - 100$ grid cells for each galaxy, with the exception of some of the barred galaxies and the ring galaxy. The reason why there are only a few grids on these galaxies is that their Σ_{H_2} values are generally low and thus many grids are discarded.

3.3 Derivation of M_{H_2} or Σ_{H_2}

For the resolved HERACLES maps, molecular gas depletion time is defined as $\Sigma_{H_2}/\Sigma_{SFR}$. We calculate the molecular gas depletion time in 1-kpc × 1-kpc grid cells. The fluxes from the reduced HERACLES CO maps are converted to Σ_{H_2} in each 1-kpc grid cell adopting the Galactic CO-to-H_2 conversion factor, 4.35 $M_\odot$ pc^{-2} (K km s^{-1})$^{-1}$. Note that we discard the bins with $\Sigma_{H_2} < 3$ $M_\odot$ pc^{-2}, which is the sensitivity limit for the HERACLES CO maps.

For the COLD GASS galaxies, the observed CO fluxes in the catalog of Saintonge et al. (2011b) are converted to the molecular gas mass. For ATLAS^{3D}, the CO flux within the Kron aperture is converted to the molecular gas mass. In both cases, the Galactic CO-to-H_2 conversion factor is used.

3.4 Derivation of SFRs or Σ_{SFR}

We estimate SFR by combining the FUV and IR data. FUV traces the emission from unobscured massive stars formed over the past ∼100Myr. UV photons absorbed by the surrounding dust cause emission at IR wavelengths. The linear combination of the FUV and IR emission can recover both the unobscured stellar emission and the dust-reprocessed emission.

3.4.1 HERACLES

We use the FUV and 24μm images to estimate Σ_{SFR}. The same method applied to the optical images is used to mask stars and background galaxies. We re-fill the masked region with the local background. We correct the FUV images for Galactic extinction using the maps of Schlegel et al. (1998). All the images are convolved to a resolution of Gaussian 13″ using the kernels released in Aniano et al. (2011).

Next we apply the method suggested in section 8.2 of Leroy et al. (2012) to remove the cirrus contribution originating from evolved stellar populations. A first-order correction is done using the total gas surface density, i.e. the sum of Σ_{H_2} and Σ_{HI}, where Σ_{HI} is obtained from THINGS data. After we remove this cirrus emission from the 24 μm emission, we then adopt the updated calibration coefficient in Leroy et al. (2012) to calculate the SFRs from the linear combination of the FUV and 24 μm luminosities. Those bins with $\Sigma_{SFR} < 10^{-3}$ $M_\odot$ yr^{-1} kpc^{-2} are excluded in the following analysis, because the SFR calibration becomes poor in the very low SFR regime (Leroy et al. 2012).

3.4.2 ATLAS^{3D}

We use the FUV and 22μm images to estimate SFRs within the aperture derived from the CO maps. Both the GALEX FUV and WISE 22μm images are convolved to 13″ resolution using the kernels from Aniano et al. (2011). The steps to process FUV and WISE 22μm images including star/background galaxy masking, sky removal, Galactic foreground extinction correction and WISE color correction, are the same as described in Huang & Kauffmann (2014).

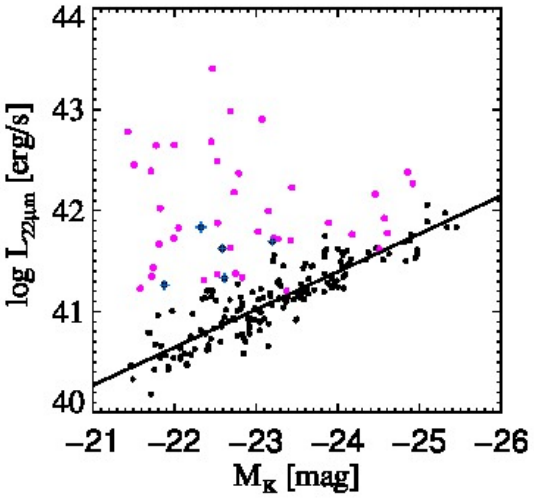

Figure 5. Relation between K-band absolute magnitude and WISE 22μm luminosity. Black and magenta solid points are the galaxies without and with CO detections from the ATLAS^{3D} sample. Only galaxies with 22μm flux S/N> 3 are shown. The black solid line is the best-fit linear regression to the CO non-detected galaxies. The blue plus symbols represent galaxies excluded during the fitting process (see text).

As the ATLAS^{3D} galaxies are ETGs, the contribution from old stellar populations to the IR emission is significant (e.g.,Kennicutt 1998). Davis et al. (2014) estimate that the average fractional contribution from evolved stars to the 22μm luminosities of ETGs is ∼25%. These authors found a tight correlation between K-band and 22μm luminosities for a subset of galaxies without CO detections and used this relation to correct the total 22μm emission for the contribution from old stars.

We retrieve 2MASS K-band Atlas images from the NASA/IPAC Infrared Science Archive for both CO-rich and CO non-detected galaxies from the ATLAS^{3D} survey. To remove stars or background galaxies, we run SEXTRACTOR and mask detected sources, with the exception of the central galaxies. We estimate the sky background as the median value of the pixels with values $< 3\sigma$ above the median value of the whole image. The K-band images are then convolved to the same 13″ resolution as the WISE 22μm images. We derive K-band and 22μm luminosities for the whole galaxy using the Kron aperture in SEXTRACTOR.

The K-band absolute magnitude is plotted against 22μm luminosity for CO-rich and CO non-detected ETGs in Figure 5. As can be seen, the K-band absolute magnitude correlates well with the 22μm luminosity for CO non-detected galaxies (black points), while there is no clear relation for the CO-rich galaxies (magenta points). We perform a linear fit to the CO non-detected galaxies and plot the result with a black solid line in Figure 5. The best-fit is given

by

$$\log(\frac{L_{22\mu m,\text{old stars}}}{\text{ergs}^{-1}}) = (-0.38 \pm 0.01) \times M_k + (32.38 \pm 0.34). \quad (1)$$

Note that there are 5 outliers (blue plus signs in Figure 5) with scatter larger than 0.5 dex. They include one galaxy with apparent spiral arms, one with a star-forming ring, one with a high HI mass fraction, and two with either a star or small galaxy nearby. We exclude these galaxies from our fits.

We measure the K-band magnitudes of CO-rich ETGs within the aperture derived from CO maps, estimate the 22μm luminosity from old stars using Equation (1), and subtract this from the total 22μm emission. We then scale the WISE 22μm fluxes so that they have the same normalization as the MIPS 24μm fluxes (Huang & Kauffmann 2014). We convert the FUV and 22μm luminosities to SFRs using the same calibration given in Leroy et al. (2012). [1]

3.4.3 COLD GASS

As in the previous section, we use GALEX FUV and WISE 22μm images to estimate SFR for COLD GASS galaxies within the central 22″ region. The procedure is the same as mentioned above. For consistency, we use the same calibration as we apply to HERACLES and ATLAS^{3D} sample to convert FUV plus 22μm into SFR.

3.5 Derivation of stellar mass

Stellar mass is derived using the SED-fitting method in Wang et al. (2011) by which the stellar population synthesis models of Bruzual & Charlot (2003) are fit to SDSS 5-band magnitudes. The parameter, sSFR, is the SFR divided by the stellar mass.

4 RESULTS

4.1 The effect of internal structures on molecular gas depletion time

4.1.1 Bulges and discs

We plot the depletion time and the ratio of $\text{SFR}_{22\mu m}$ to SFR_{FUV} (IR/UV) as a function of radius for bulge and disc grids in Figure 6. Whereas the depletion time of the bulge grids drops towards the center of the galaxy, the depletion time of the disc grids remains almost constant as a function of radius. In contrast, the IR/UV ratios of the disc and bulge grids decline from the center towards the outskirts – this is not surprising because the IR/UV ratio is a robust indicator of dust attenuation, and the outer parts of galaxies are expected to have lower metallicities and dust content. We note that the fact that different radial trends are found for depletion time and for IR/UV ratio make it seem unlikely that variations in CO-to-H_2 conversion factor are responsible for the drop in the depletion time in the central bulge. We note that this result is consistent with results presented in Leroy et al. (2013) (see Section 5 for further discussion).

4.1.2 COLD GASS

As in the previous section, we use GALEX FUV and WISE 22μm images to estimate SFR for COLD GASS galaxies within the central 22″ region. The procedure is the same as mentioned above. For consistency, we use the same calibration as we apply to HERACLES and ATLAS^{3D} sample to convert FUV plus 22μm into SFR.

4.2 Derivation of stellar mass

Stellar mass is derived using the SED-fitting method in Wang et al. (2011) by which the stellar population synthesis models of Bruzual & Charlot (2003) are fit to SDSS 5-band magnitudes. The parameter, sSFR, is the SFR divided by the stellar mass.

5 RESULTS

5.1 The effect of internal structures on molecular gas depletion time

5.1.1 Bulges and discs

We plot the depletion time and the ratio of $\text{SFR}_{22\mu m}$ to SFR_{FUV} (IR/UV) as a function of radius for bulge and disc grids in Figure 6. Whereas the depletion time of the bulge grids drops towards the center of the galaxy, the depletion time of the disc grids remains almost constant as a function of radius. In contrast, the IR/UV ratios of the disc and bulge grids decline from the center towards the outskirts – this is not surprising because the IR/UV ratio is a robust indicator of dust attenuation, and the outer parts of galaxies are expected to have lower metallicities and dust content. We note that the fact that different radial trends are found for depletion time and for IR/UV ratio make it seem unlikely that variations in CO-to-H_2 conversion factor are responsible for the drop in the depletion time in the central bulge. We note that this result is consistent with results presented in Leroy et al. (2013)

In Figure 7, we investigate the t_{dep}−sSFR relation for bulges (blue solid points) and discs (grey solid points) regions. We also plot the ATLAS^{3D} bulge-dominated sample for comparison (red solid points). We perform OLS-bisector fits to the data and plot the fitting results in Figure 7 as well. There are two obvious results: First, the scatter in depletion time is larger in bulges than in discs (0.33 dex in $\log t_{dep}$, compared to 0.22 for discs). Excluding bulge grids with $R < 0.1\ R_e$, which may be influenced by AGN , makes no difference to this conclusion. Second, in the bulge, t_{dep} is systematically shifted to smaller values at a given sSFR compared to the disc grids. We note that there are some bulge grids whose depletion times lie above the grey line derived for disc grids in Figure 7. We check the location of these grids and find that they are generally in the outer region of the bulge.

[1] We note that the local calibrations may not be applicable to global conditions (Calzetti et al. 2013), so we also try the calibration formula given in Hao et al. (2011) which is derived for the whole galaxy. We find that this makes little difference to our results.

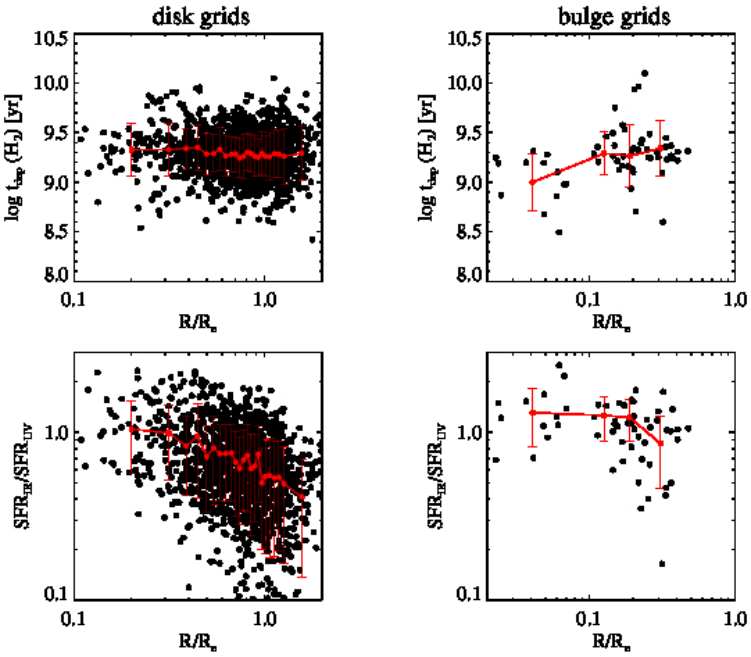

Figure 6. Molecular gas depletion time (upper panel) and the IR/UV ratio (lower panel) as a function of radius for disc and bulge grids of HERACLES sample. The radius is normalized to the effective radius of the disc, R_e.

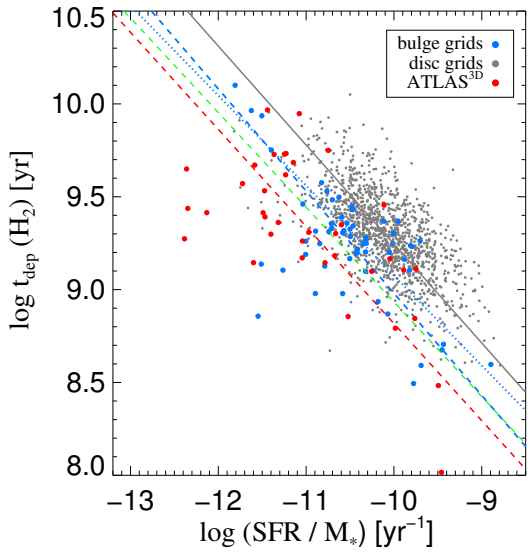

Figure 7. t_{dep}− sSFR relation for the bulge and disc grids of the HERACLES sample, as well as the ATLAS^{3D} galaxies. Grey and blue solid points show grids in the disc and bulge regions of the HERACLES galaxies. Red solid points show the ATLAS^{3D} sample. OLS bisector fits to the disc, bulge and ATLAS^{3D} data points are shown as grey, blue, and red dashed lines. The blue dotted line shows the OLS bisector fit to the bulge grids, excluding those those with R $< 0.1R_e$. The green dashed line is the OLS bisector fit to the HERACLES bulge data points plus the results from the ATLAS^{3D} sample.

5.1.2 Spiral arms, bars and rings

In Figure 8, we plot the t_{dep}−sSFR relation for galaxies with grand-design arms, bars and rings. Magenta points denote the grids located within the region of the targeted structure, such as the grand-design arm, bar or ring; blue points denote other grids in the same galaxies. Grids from other galaxies, i.e. those galaxies that do not contain the designated structure, are shown in grey.

The sSFRs in the interstellar medium (ISM) of galaxies with grand-design arms are higher than in galaxies without arms, and the sSFRs within the arms themselves are the highest. This is expected, because gas is compressed by spiral density waves and star formation rate scales with gas surface density. Interestingly, t_{dep} is shifted to higher values at a given sSFR in galaxies with spiral arms. We apply OLS-bisector fits to the spiral arm data and the results are shown as dashed lines in Figure 8. Indeed, the grids in the regions with (blue dashed line) or without (magenta dashed line) arms are systematically shifted to longer t_{dep} at fixed sSFR compared to the grey dashed line, which is for galaxies without spiral structure.

In barred galaxies, we find the opposite trend. The sSFRs in the interstellar medium of galaxies with bars (magenta points in the middle panel) are much lower than in galaxies without bars. Bars are long-lived structures. Although they can act to channel gas towards the center of a galaxy and fuel starbursts, this is a transient phenomenon and the majority of present-day barred galaxies are relatively quiescent. The OLS-bisector fit to the grids in barred galaxies indicates that t_{dep} is shortened at fixed sSFR compared to grids from galaxies without bars. This is exactly the opposite to what was found for galaxies with spiral arms. There is only one galaxy with a ring in HERACLES sample,

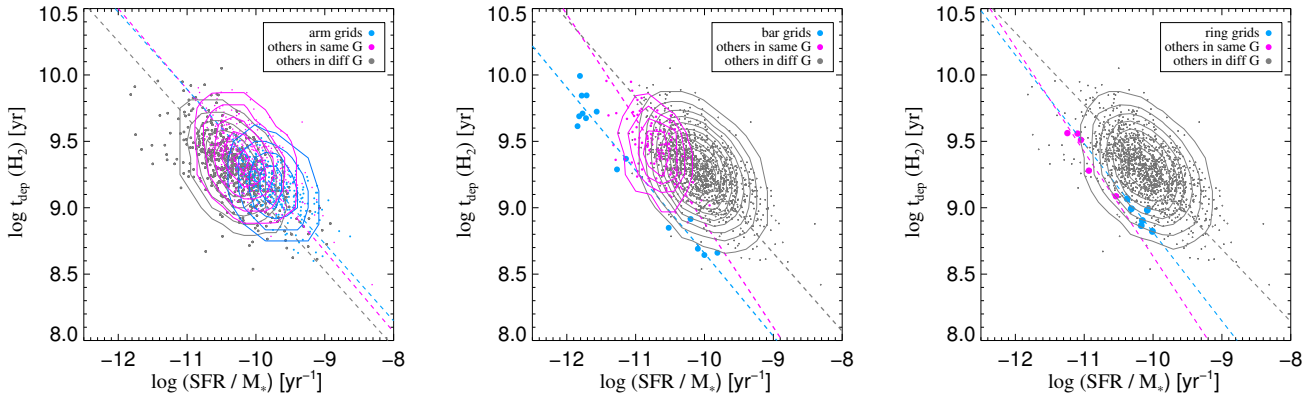

Figure 8. Distribution in the $t_{dep}-$ sSFR plane of grids in galaxies with spiral arms (left), in galaxies with bars (middle) and in galaxies with rings (right). Results for grids within the arm, bar or ring regions are coloured in blue. Results for grids in these galaxies outside the arms,bars or rings are coloured in magenta. Results for grids in galaxies without arms, bars or rings are coloured in grey. OLS-bisector fits to the data points in these different groups are shown with the same color.

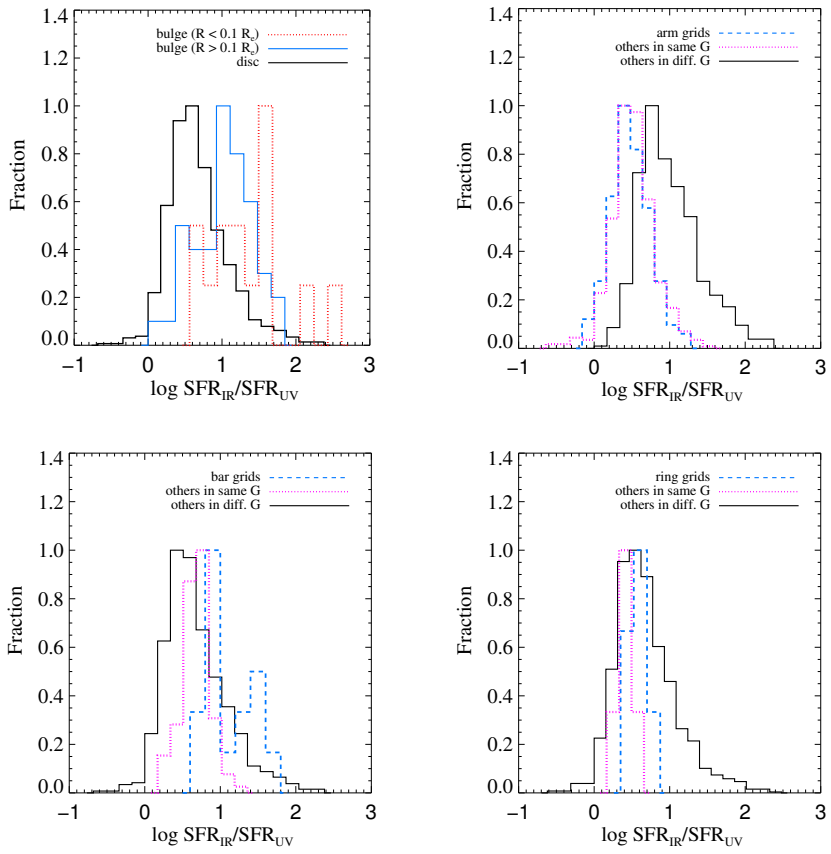

Figure 9. Distribution of the ratio of $SFR_{22\mu m}$ to SFR_{FUV}. In the upper left panel, red dashed and blue histograms show results for grids in the bulge regions with R $< 0.1R_e$ and R $> 0.1R_e$ respectively. The black histogram is for the grids in the disc regions. In the other panels, blue histograms are for grids within the structure (arm or bar or ring); magenta histograms are for the grids outside the structure; black histograms are for the grids from the other galaxies in the HERACLES sample. Upper right panel: the spiral-arm galaxies. Lower left and right panels: the barred and ring galaxies.

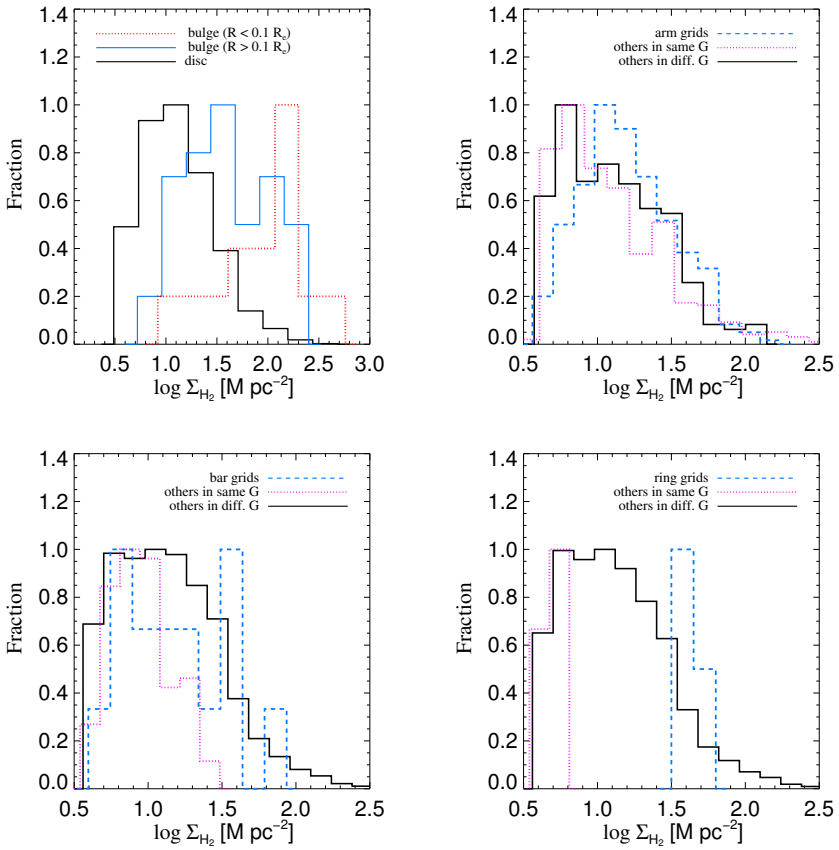

Figure 10. Distribution of the molecular gas surface densities. Conventions and lines are as in Figure 9.

so we only have a few grids available for analysis. Based on the limited data, we conclude that ringed galaxies follow the same trends as barred galaxies.

5.2 Linking the results together

So far, we have analyzed molecular gas depletion time variations in terms of location within or outside specific structures of the galaxy, such as bulges, bars, arms or rings. We now ask whether all of these variations can be linked to a physical parameter that varies continuously within galaxies. For example, Daddi et al. (2010) and Genzel et al. (2010) proposed that the combination of high gas density and short dynamical timescale could explain the short global molecular gas consumption timescales in strongly starbursting galaxies. The parameters that we examine in this section are, 1) IR/UV ratio as a proxy for dust content, 2) H_2 surface density, 3) stellar surface density.

IR/UV ratio In Figure 9, we plot the distributions of IR/UV ratios for inner bulge, outer bulge and disk grids in the top left panel. In the top right panel, we plot distributions for spiral arm, inter-arm and control grids. The bottom two panels are the same as the top right panel, except that results are shown for bars and rings.

As we have seen previously, IR/UV ratios are highest in the inner regions of bulges, from which we infer that these are the dustiest regions of nearby galaxies. The high dust content in the centers of bulges means that it is unlikely that we have under-estimated the H_2 content on the galaxy by using the Galactic CO-to-H_2 conversion factor. The short depletion times observed in central bulges are thus not likely to be an artifact of wrongly estimated molecular gas masses. The least dusty regions of the ISM are found within galaxies with grand-design spiral arms. By a similar argument, we infer that that higher molecular gas depletion times observed in these regions are not likely to be an artifact of conversion factor variations either.

Grids within bars in barred galaxies have similar IR/UV ratio as the outer parts of galactic bulges, while those outside bars have IR/UV ratios similar to the general disc population. Grid within rings appear less dusty than grids within bars, but we caution that our sample consistent of only one ringed system.

In summary, we deem it unlikely that variations in CO-to-H_2 conversion factor are responsible for the different t_{dep}−sSFR relations among grid cells lying within different structures.

H_2 surface density Figure 10 is the same as Figure 9, except that distributions of H_2 surface density are shown. If we exclude the single ringed galaxy, the only significant shift in H_2 surface density occurs within bulges, which have molecular gas densities up to a factor of 30 higher than discs, particularly in their inner regions. The enhancement in gas density in the grids with spiral arms is only about 50%, and grids that lie outside spiral arms have H_2 densities that are identical to grids with galaxies without arms. Gas density is

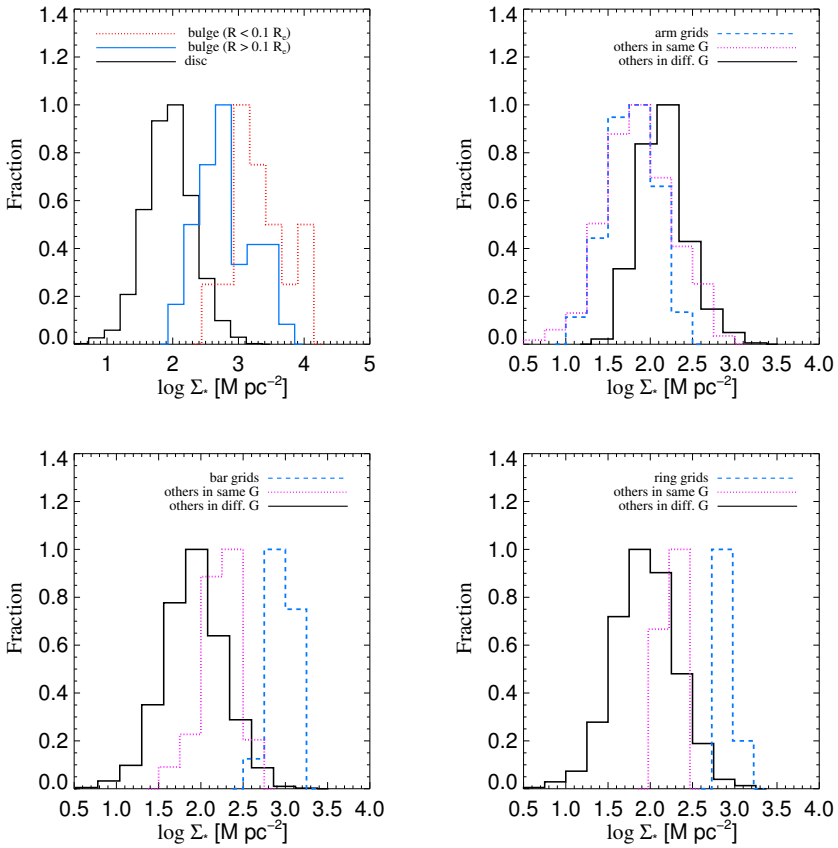

Figure 11. Distribution of the stellar surface densities. Conventions and lines are as in Figure 9.

enhanced more strongly within bars, but still not as strongly as in bulges.

In conclusion, although high gas densities may be a promising avenue for explaining the short depletion time in bulges and starburst systems, it does not appear to vary in a systematic way in other environments such as spiral arms and bars, so as to explain other observed trends. We will demonstrate this in more detail later in this section.

Stellar surface density In Figure 11, we plot the distributions of stellar surface density for the grids within different structures. In this case, there is a very clear separation between grid cells in bulges, bars and rings, which peak at log $\Sigma_* \sim 3$ $M_\odot$ pc^{-2} while grids in the spiral-arm galaxies peak at log $\Sigma_* \sim 1.5-2$ $M_\odot$ pc^{-2}. Grids in the inner regions of bulges, where t_{dep} is shortest, are shifted to even higher Σ_* than the outer bulges. Spiral arm and inter-arm grids also peak at lower Σ_* values than grids from galaxies without spiral arms. In summary, variations in the Σ_* distributions between different galaxy structures mirror the variations in the t_{dep}-sSFR relations described in the previous section extremely well.

We now fit a linear relation to the $t_{dep}-$sSFR relation for all grid data points and plot the residuals against Σ_*, Σ_{H_2} and a third quantity, the interstellar pressure, in Figure 12. Following Leroy et al. (2008), the pressure, P_h, is expressed as

$$P_h \approx \frac{\pi}{2} G \Sigma_{gas} (\Sigma_{gas} + \frac{\sigma_g}{\sigma_{*,z}} \Sigma_*), \quad (2)$$

where σ_g and $\sigma_{*,z}$ are velocity dispersions of gas and stars, and Σ_{gas} and Σ_* are the gas and stellar surface densities. Data from ATLAS^{3D} and COLD GASS are also added in this figure.

Figure 12 shows that Σ_* is the only quantity that clearly correlates with Δt_{dep}. Grids in bulges, bars, and rings and the ATLAS^{3D} sample clearly separate from the spiral arm, inter-arm and disc grids in this plot. We can also understand the reason why we did not observe a correlation between Δt_{dep} and Σ_* for the COLD GASS sample in Huang & Kauffmann (2014) : the dynamic range in Σ_* of the COLD GASS sample is too small. The integrated stellar surface densities of the COLD GASS sample span only 1 dex on the x-axis.

Motivated by these results, we fit a plane to the two-dimensional relation between the depletion time, specific star formation rate and the stellar surface density. Following the method in Bernardi et al. (2003), we find the best-fit linear correlation of the form

$$t_{dep} = a \log(sSFR) + b \log(\Sigma_*) + c \quad (3)$$

We plot all the data, including the grids from HERACLES, the ATLAS^{3D} sample and the COLD GASS sample in Figure 13, and we show the $t_{dep}-$sSFR relation in the next panel for comparison. The 1:1 relation is shown by a black solid line. The values of the coefficients, a, b, and c from the best-fit result are -0.36, -0.14, and 5.87 respectively. The Pearson linear correlation coefficient r between the x

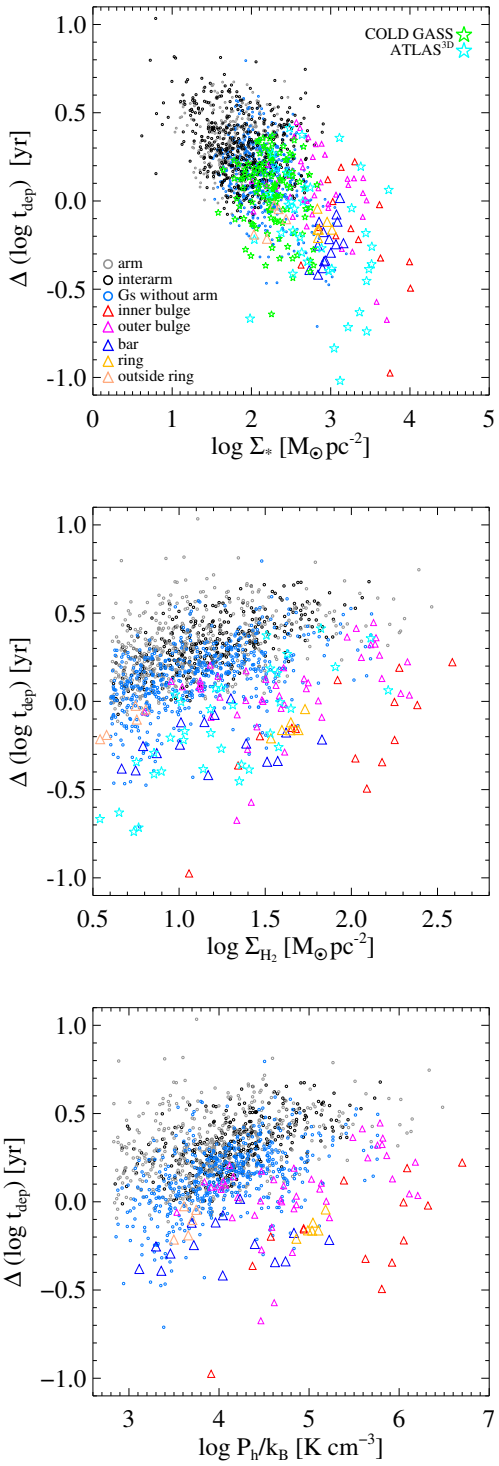

Figure 12. Residuals from the $t_{dep}-$ sSFR relation as a function of Σ_* (top panel), Σ_{H_2} (middle panel), and midplane gas pressure (bottom panel). Grey and black circles are the grids in and outside the arm regions of the spiral galaxies from HERACLES. Light blue circles denote grids from galaxies without spiral-arms. Blue and yellow triangles denote the grids in the bars and the ring. Beige triangles denote the grids from the ring galaxy but outside the ring region. Cyan and green stars represent the ATLAS^{3D} and COLD GASS sample respectively.

and y axes is 0.68, and the scatter in t_{dep} about the plane is 0.18 dex. The reduction in scatter, compared to the one-dimensional relation for t_{dep} versus sSFR, which has a scatter of 0.19, is only 5%. This is because our sample is heavily dominated by the number of grids from the disc-dominated regions of galaxies. The main effect of the two-parameter fit is to bring the outlying points, which are mainly from bulge and bar grid cells, into better agreement with the rest of the sample.

Finally, we note that for 1 kpc^2 grid cells, we can rewrite equation (3) above as

$$t_{dep} = a\log(\Sigma_{\rm SFR}) + (b-a)\log(\Sigma_*) + c \qquad (4)$$

This means that the surface density of evolved stars in a grid cell contributes ∼1.4 times more weight to our prediction of depletion time than the surface density of newly formed stars! We will speculate on possible reasons for this in the next section.

6 SUMMARY AND DISCUSSION

Using the resolved maps of the nearby HERACLES galaxies, we have calculated the molecular gas depletion time in 1-kpc × 1-kpc grid cells and studied the $t_{dep}-$sSFR relation for grids lying within different galaxy structures such as bulges, arms, bars, and rings.

Our main results can be summarized as follows:

(i) Bulge regions have shorter gas depletion times than the disk regions at a given value of the sSFR. This effect is strongest in the central regions of the bulge.

(ii) The $t_{dep}-$sSFR relation for the grid cells in spiral-arm galaxies shifts to longer t_{dep} at fixed sSFR compared to grid cells from galaxies without spiral arms. Note that this shift applies to *all grid cells* from spiral arm galaxies. Within a spiral arm, the sSFR values are higher than in the inter-arm region, so the average depletion times will be shorter.

(iii)Grid cells located within bars have reduced depletion time at fixed sSFR. Grids located in barred galaxies outside of the barred region occupy a narrow range of low sSFR values.

(iv) We identify the stellar surface density Σ_* as the parameter that can best predict the shifts between the relations found for bulges, bars and spiral arms.

Our results on star formation efficiencies in spiral arms are largely consistent with those presented in Figure 7 of Foyle et al. (2010) and Figure 13 of Rebolledo et al. (2013) even though our methodology for identifying spiral arms differs from these papers. Several previous papers have claimed that star formation efficiencies in bars are low (e.g., Reynaud & Downes 1998; Momose et al. 2010 ; Sorai et al. 2012). We note that in our sample, the molecular gas depletion time in barred regions spans a range of more than a factor of 10. Only in bars with high gas densities do we find grid cells with short depletion times and high SFEs. This is consistent with the work of Sheth et al. (2005), who find that barred spiral galaxies generally have higher molecular gas concentrations in their central regions. However, barred galaxies exist that have no molecular gas detected in the nuclear region and

very little within the bar corotation radius. Bars are long-lives, and we likely observe them at different evolutionary stages, which explains why the SFE has such a large spread.

Our result that bulge grids have reduced depletion time compared to disc grids is consistent with results presented in Leroy et al. (2013). These authors studied radial trends in molecular gas depletion time as a function of radius and observed that the average t_{dep} was smaller in the central $\sim$1kpc regions. The reduced depletion time was even more pronounced after they applied a CO-to-H_2 conversion factor that depended on dust-to-gas ratio. Once again, these authors did not study trends of depletion time at fixed specific star formation rate.

We note that Davis et al. (2014) found that star formation efficiencies (SFEs) of the ETGs in ATLAS^{3D} survey were *reduced* compared to spiral galaxies. The main reason for this apparently discrepant result is the definition of star formation efficient adopted by these authors: SFE was computed as the ratio of the total (atomic+molecular) gas mass divided by the total star formation rate of the galaxy. The analysis in this paper only considers the star formation efficiency of the molecular gas component of the galaxy. We note that *no previous study has considered variations in SFE at fixed specific star formation rate*, which is the main focus of this paper

Why should the star formation efficiency of the molecular gas be so sensitive to the local surface density of evolved stars? Helfer & Blitz (1993) studied the properties of the dense molecular gas in the bulges of a sample of 19 normal spiral galaxies. They observed the 3mm emission from the molecules HCN and CS, which traces much denser gas than CO. They found that the CS to CO ratio in the external bulges was consistent with that measured for the bulge of the Milky Way and a factor of 2 or more larger than in the Galactic disc. In subsequent work, Helfer & Blitz (1997) carried out interferometric observations of emission from the HCN molecule in NGC 6946, NGC 1068, and the Milky Way and found that the ratio of HCN to CO at the galactic centres was 5-10 times higher than in the discs of these galaxies.

Helfer & Blitz (1993) put forward two possible explanations for their findings: 1) Because the stellar potential is larger in the bulge than in the disc, the gas is subject to much higher pressures, 2) The giant molecular clouds (GMCs) have different mass and/or structure in the bulge than in the disc. Launhardt, Zylka & Mezger (2002) emphasized that most of the ISM in the central bulge of the Milky Way is likely in the form of very dense, compact clouds. These conclusions arise from the lack of a significant diffuse component in high resolution submm maps of the Galactic centre. They speculate that the physical reason for the observed clumpiness of the ISM is the tidal stability limit – clouds have to be dense enough to be stabilized against tidal forces by their own gravitation.

The results in this paper suggest that there may be a *continuum* of molecular cloud properties set by the local stellar surface density. If so, this would have very interesting consequences for our understanding of galaxy evolution. Gas-to-evolved star ratios are much higher in the early Universe than they are today (Tacconi et al 2010) and star formation may likewise be proceeding in a quite different manner inside GMCs.

ACKNOWLEDGMENTS

We thank Linda Tacconi, Reinhard Genzel, Jing Wang, Richard D'Souza, Sambit Roychowdhury for helpful discussions.

GALEX is a NASA Small Explorer, launched in 2003 April, developed in cooperation with the Centre National d'Etudes Spatiales of France and the Korean Ministry of Science and Technology.

This research has made use of the NASA/IPAC Infrared Science Archive, which is operated by the Jet Propulsion Laboratory, California Institute of Technology, under contract with the National Aeronautics and Space Administration.

Funding for the SDSS and SDSS-II has been provided by the Alfred P. Sloan Foundation, the Participating Institutions, the National Science Foundation, the US Department of Energy, the National Aeronautics and Space Administration, the Japanese Monbukagakusho, the Max Planck Society, and the Higher Education Funding Council for England. The SDSS is managed by the Astrophysical Research Consortium for the Participating Institutions. The Participating Institutions are the American Museum of Natural History, Astrophysical Institute Potsdam, University of Basel, Cambridge University, Case Western Reserve University, University of Chicago, Drexel University, Fermi National Accelerator Laboratory, the Institute for Advanced Study, the Japan Participation Group, Johns Hopkins University, the Joint Institute for Nuclear Astrophysics, the Kavli Institute for Particle Astrophysics and Cosmology, the Korean Scientist Group, The Chinese Academy of Sciences (LAMOST), the Leibniz Institute for Astrophysics, Los Alamos National Laboratory, the Max-Planck-Institute for Astronomy (MPIA), the Max-Planck-Institute for Astrophysics (MPA), New Mexico State University, Ohio State University, University of Pittsburgh, University of Portsmouth, Princeton University, the US Naval Observatory and the University of Washington.

REFERENCES

Aniano G., Draine B. T., Gordon K. D., Sandstrom K., 2011, PASP, 123, 1218
Alatalo K. et al., 2013, MNRAS, 432, 1796
Bernardi M. et al., 2003, AJ, 125, 1866
Bigiel F., Leroy A. K., Walter F., Brinks E., De Blok W. J. G., Madore B., Thornley M. D., 2008, AJ, 136, 2846
Bigiel F. et al., 2011, ApJ, 730, L13
Bruzual G., Charlot S., 2003, MNRAS, 539, 718
Calzetti D., 2013, Star Formation Rate Indicators. Cambridge Univ. Press, Cambridge, p. 419
Cappellari M. et al., 2011, MNRAS, 413, 813
Daddi E. et al., 2010, ApJL, 714, 118
Davis T. A. et al., 2014, MNRAS, 444,3427
Dib S., Helou G., Moore T. J. T., Urquhart J. S., Dariush A., 2012, ApJ, 758, 125
Eden D. J., Moore T. J. T., Morgan L. K., Thompson M. A., Urquhart J. S., 2013, MNRAS, 431, 1587
Foyle K., Rix H.-W., Walter F., Leroy A. K., 2010, ApJ, 725, 534
Fujimoto Y., Tasker E. J., Habe A., 2014, MNRAS, 445, L65

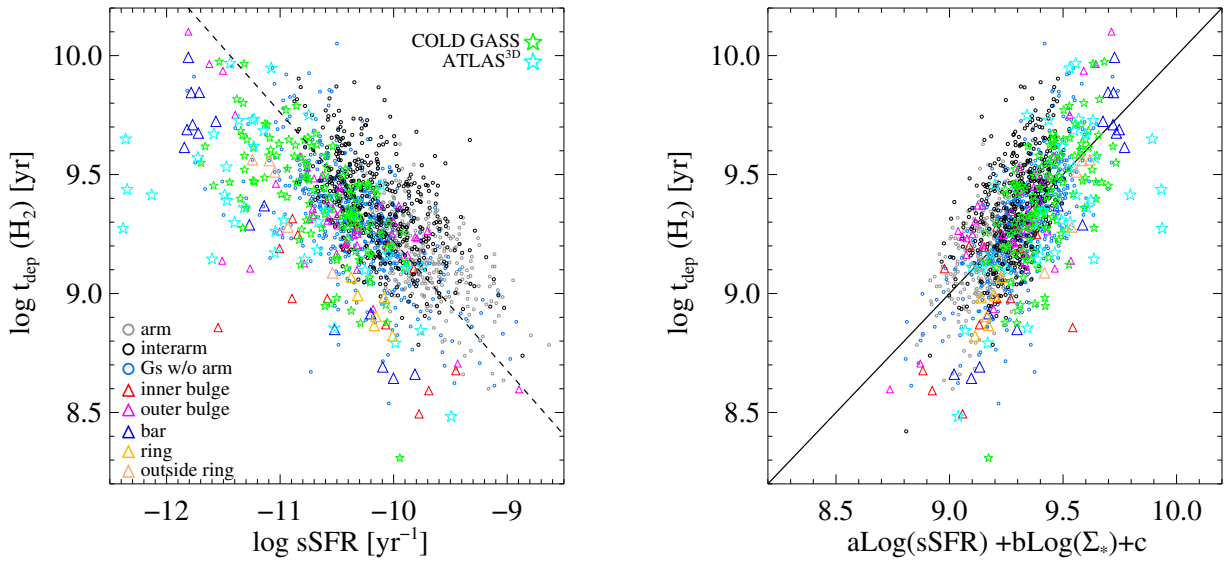

Figure 13. Left panel: $t_{dep}-$ sSFR relation for all grids of the HERACLES sample ,ATLAS^{3D} galaxies, and the COLD GASS galaxies. Grey and black circles are the grids in and outside the arm regions of the spiral galaxies from HERACLES. Light blue circle denote grids from galaxies without spiral-arms. Blue and yellow triangles denote the grids in bars and rings. Beige triangles denote the grids from the ring galaxy but outside the ring region. Cyan and green stars represent the ATLAS^{3D} and COLD GASS sample separately. We show the OLS bisector fit to all grid data from the HERACLES sample with a black dashed line. Right panel: The best-fit plane linking t_{dep}, sSFR, and Σ_*. Symbols are as in the left plot. The best-fit coefficients, a, b, c, are -0.36, -0.14, 5.87 respectively.

Gadotti D. A. et al., 2009, MNRAS, 393, 1531
Genzel R. et al., 2010, MNRAS, 407, 2091
Genzel R. et al., 2015, ApJ, 800, 20
Gil de Paz A. et al., 2007, ApJS, 173, 185
Hao C.-N., Kenicutt R. C. Jr., Johnson B. D., Calzetti D., Dale D. A., Moustakas J. ,2011, ApJ, 741, 124
Helfer T. T., Blitz L., 1993, ApJ, 419, 86
Helfer T. T., Blitz L., 1997, ApJ, 478, 162
Hirota A. et al., 2014, PASJ, 66, 46
Huang M.-L., Kauffmann G., 2014, MNRAS, 443,1329
Kennicutt R. C. Jr., 1998, ARA&A, 36, 189
Kennicutt R. C. Jr. et al., 2003, PASP, 115, 928
Knapen J. H., Beckman J. E., Cepa J., Nakai N., 1996, A&A, 308, 27
Launhardt R., Zylka R., Mezger P. G., 2002, A&A, 384, 112
Leroy A. K. et al., 2008, AJ, 136, 2782
Leroy A. K. et al., 2012, AJ, 144,3
Leroy A. K. et al., 2013, AJ, 146,19
Lord S. D., Young J. S., 1990, ApJ, 356, 135
Muñoz-Mateos et al., 2009, ApJ, 703,1569
Meidt S. E. et al., 2013, ApJ, 779, 45
Momose R., Okumura S. K., Koda J., Sawada T., 2010, ApJ, 721, 383
Momose R. et al., 2013, ApJ, 772, L13
Pan H.-A., Kuno N., Hirota A., 2014, PASJ, 66, 27
Peng C. Y., Ho L. C., Impey C. D., Rix H.-W. et al., 2002, AJ, 124,266
Rebolledo D., Wong T., Leroy A., Koda J., Meyer D. J., 2012, ApJ, 757, 155
Reynaud D., Downes D., 1998, A&A, 337, 671
Saintonge A. et al., 2011a, MNRAS, 415, 32
Saintonge A. et al., 2011b, MNRAS, 415, 61
Saintonge A. et al., 2012, ApJ, 758, 73
Schlegel D. J., Finkbeiner D. P., Davis M., 1998, ApJ, 500,525
Schmidt M., 1959, ApJ, 129, 243
Sheth K., Vogel S. N., Regan M. W., Thornley M. D., Teuben P. J., 2005, ApJ, 632, 217
Shetty R., Kelly B. C., Bigiel F., 2013, MNRAS, 430, 288
Sorai K. et al., 2012, PASJ, 64, 51
Tacconi L. J. et al., 2010, Nature, 463, 781
Walter F., Brinks E., de Blok W. J. G., Bigiel F., Kennicutt R. C. Jr., Thornley M. D., Leroy A. K., 2008, AJ, 136, 2563
Wang J. et al., 2011, MNRAS, 412, 1081
Weinmann S. M., Kauffmann G., van den Bosch F. C., Pasquali A., McIntosh D. H., Mo H., Yang X., Guo Y., 2009, MNRAS, 394, 1213
Young L. M. et al., 2011, MNRAS, 414, 910